DFUB 95-26

RESULTS FROM ACCELERATOR EXPERIMENTS

GIORGIO GIACOMELLI
Physics Department, University of Bologna and INFN, V.le B.Pichat 6/2
40127, Bologna, Italy
E-mail: giacomelli@bo.infn.it

and

ROBERTO GIACOMELLI
Physics Department, University of Bologna and INFN, V.le B.Pichat 6/2
40127, Bologna, Italy
E-mail: giacomellir@bo.infn.it

Lectures at the 4th School on Non-Accelerator Particle Astrophysics
Trieste, 17-28 July 1995

ABSTRACT

Recent experimental results obtained at high-energy accelerators are reviewed. The main emphasis is on collider experiments, at LEP and SLC for e^+e^- collisions, Fermilab for $\bar{p}p$ collisions, and HERA for ep collisions.

1. Introduction

The development of particle physics is intimately connected with the development of accelerators of ever-increasing energies which can explore smaller and smaller distances. In the last 20 years experimental high-energy physics has moved from fixed target accelerators to colliders, the most common being the e^+e^- type. The first e^+e^- colliders were made in the 1960's and they quickly increased in number and in energy. The existing largest e^+e^- colliders are the LEP storage ring at CERN and the SLC linear collider at SLAC. They have provided a wealth of information at energies around the Z^0 mass and tested the Standard Model (SM) of electroweak and strong interactions to high precision. LEP will soon be upgraded to ~190 GeV c.m. energy.

The first pp collider, the ISR at CERN, started operation in the 70's at c.m. energies up to 63 GeV. This accelerator started the field of parton-parton scattering and systematized the low p_t-physics field.

In the early 80's the CERN SPS was modified to become a $\bar{p}p$ collider which soon led to the discovery of the $W^\pm$ and Z^0 bosons. In the late 80's the Tevatron collider ($\sqrt{s}$=1800 GeV) started operation. Recently it obtained evidence for the top quark and also measured total $\bar{p}p$ cross-sections at the highest energies.

The asymmetric ep collider HERA started operation in 1992 with a 27 GeV e^+ beam and a 820 GeV p beam ($\sqrt{s}$ = 296 GeV). It allows the study of deep inelastic scattering at very low values of the Bjorken x variable and at very high Q^2. It was

soon found that the parton densities in the proton rise rapidly as $x \to 0$.

In these lectures notes the main recent results from LEP, SLC, Tevatron and HERA will be briefly discussed; some results will also be reported from lower energy accelerators.

2. Colliders

In fixed-target accelerators the c.m. energy, $E_{\rm cm} = \sqrt{s}$, grows with the square root of the beam energy E_b : $s \simeq 2m_p E_b$, where m_p is the mass of the target particle. In colliders however the c.m. energy grows linearly with the beam energy: $\sqrt{s} = 2E_b$. All existing high-energy accelerators are colliders and a list is given in Table 1. While there is only one ep and one $\bar{\rm p}$p collider, there are several $\rm e^+e^-$ colliders operating at different energies. The largest $\rm e^+e^-$ collider is LEP, where the c.m. energy will soon be raised from 90 GeV to about 190 GeV. Synchrotron radiation limits the maximum energy in an $\rm e^+e^-$ collider: in the future this will probably be overcome with linear $\rm e^+e^-$ colliders. Fig. 1 shows the energy dependence of the cross-sections for $\rm e^+e^- \to$ hadrons and $\rm e^+e^- \to \mu^+\mu^-$ up to $\sqrt{s} = 1000$ GeV.

The existing largest energy collider is the $\bar{\rm p}$p collider at Fermilab, $\sqrt{s} = 1.8$ TeV. At CERN the Large Hadron pp Collider (LHC) has recently been approved: it is planned for $\sqrt{s} = 14$ TeV.

Besides energy, the second important parameter of a collider is its luminosity $\mathcal{L}$, which is defined as that number which multiplied by a cross-section σ gives the collision rate N : $N = \mathcal{L}\sigma$. Existing colliders have luminosities in the range $10^{31} < \mathcal{L} < 10^{32}$ cm^{-2} s^{-1}, which yield collision rates of $\sim$ 1 event/s at LEP and $\sim 10^6$ events/s at the $\bar{\rm p}$p collider at Fermilab. It should be remembered that fixed targed hadron accelerators easily yield luminosities of the order of 10^{35} cm^{-2} s^{-1}. Thus existing colliders provide high energy and relatively low luminosities. LHC should circumvent the luminosity limitation: it should be able to provide luminosities in the range $10^{33} - 10^{34}$ cm^{-2} s^{-1}.

All existing colliders are equipped with large general-purpose 4π detectors with tracking chambers in a magnetic field, electromagnetic and hadron calorimeters, muon detectors and luminosity monitors. Some small specialized experiments are also performed, such as the total cross-section experiments at Fermilab.

3. LEP results

In the period 1989-1995, each of the four experiments at LEP-1 (ALEPH, DELPHI, L3, and OPAL) recorded about 4.5 million events, corresponding to an integrated luminosity of about 160 pb^{-1}. It has to be remembered that at $\sqrt{s} \sim m_Z$ the cross-sections are large, see Fig. 1. LEP has been working at energies at or around the Z^0 mass (this phase is usually referred to as LEP-1 or LEP-100). Since the Z^0 is

Table 1. Current high energy colliders. The table gives the colliding beam energies in GeV. A pp (0.4×0.4 TeV) and nucleus-nucleus collider is being built at Brookhaven. Recently the LHC pp collider has been approved at CERN : it should have $E_{cm} = 14$ TeV. e^+e^- colliders have been approved at Frascati (DaΦne at m_Φ) and at SLAC (at m_Υ).

e^+e^-	GeV	ep	GeV	$\bar{p}p$	GeV
Beijing	2×2	HERA	27×820	Tevatron	900×900
Cornell	5×5				
TRISTAN	32×32				
SLC	46×46				
LEP-1	46×46				
LEP-2	$> 90 \times 90$				

a carrier of the weak force, the precise measurements of its mass, width, and decay properties are precision tests of the electroweak theory. The mass of the Z^0 is a fundamental parameter of this theory. The width of the Z^0 peak is a measure of the Z^0 lifetime. In the Standard Model the Z^0 decay width is related to the number of fermion pairs into which the Z^0 can decay. The more ways in which it can decay, the faster it decays and the wider the Z^0 peak becomes. A precise measurement of the Z^0 width constrains the number of generations, and deviation from an integer value will hints at new physics.

Radiative corrections modify the Breit-Wigner shape of the Z^0 resonance, reducing its height by 30%, shifting its position a little, and making it slightly asymmetric.

Since the Z^0 decays predominantly into quark-antiquark pairs, it yields a clean data sample with which to test quantum chromodynamics (QCD), the theory of the strong interaction. The quark-antiquark pair is never observed directly, but it gives rise to two opposite jets of hadrons by a process called fragmentation. Before fragmentation takes place, one of the quarks may radiate a gluon by a process similar to bremsstrahlung. In this case, three jets of hadrons are produced. The ratio of the number of three-jet events to the number of two-jet events is one way of measuring α_s, the strong coupling constant, which is a fundamental parameter of QCD.

The analyses of radiative corrections yielded a precise value for the top-quark mass, in excellent agreement with the recently measured value.

In addition to the vector bosons (carriers of the interactions), the quarks and the leptons, the SM requires at least one scalar Higgs particle (the H^0), which is needed for the hypothesized mechanism for the generation of masses. The coupling of the Higgs particle is predicted by the theory, but not its mass. The precision measurements at the Z^0, yield limits on the H^0 mass, limits which will become more stringent with the 1995 data and the new measurements of the t and $W^\pm$ masses.

Searches for new physics include searches for supersymmetric particles, charged Higgs bosons, substructures of quarks and leptons, excited leptons, tests of various conservation laws, and so on.

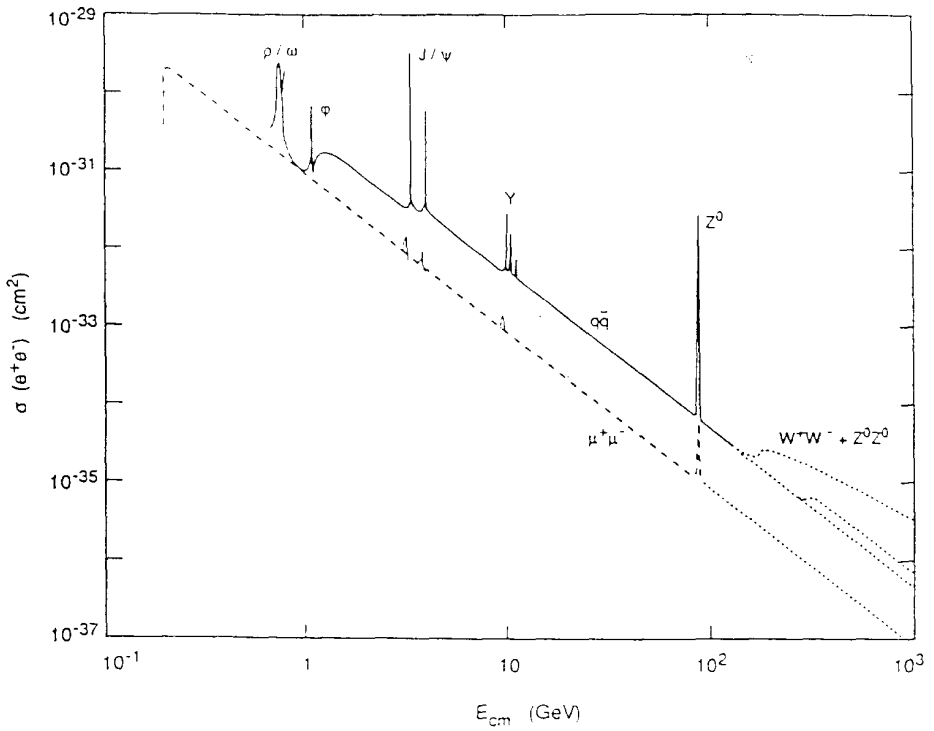

Fig. 1. Energy dependence of $\sigma(e^+e^- \to \text{hadrons})$ and $\sigma(e^+e^- \to \mu^+\mu^-)$.

3.1. LEP and the four detectors at LEP

LEP is an e^+e^- circular collider, with a circumference of 27 km, and circulating beams of about 1 mA in four e^+ and four e^- bunches. In each of the four interaction regions the bunches collide every 23 μs.

The standard setting-up procedure for LEP is as follows: a high-intensity beam of electrons, accelerated to 200 MeV, hits a high-Z target, where positrons are produced. The positrons are accelerated to 600 MeV in the LEP Injector Linacs (LIL). In the early runs the positrons were accumulated in eight bunches in the Electron–Positron Accumulator (EPA), where they are "naturally" cooled by synchrotron radiation. The positrons are then transferred to the Proton Synchrotron (PS), where they are accelerated to 3.5 GeV. Then the Super Proton Synchrotron (SPS) accelerates them to 20 GeV. The eight bunches are finally transferred to the LEP ring where they are reassembled into four bunches. This procedure is repeated for electrons (600 MeV in LIL, then 3.5 GeV in the PS in the opposite direction, 20 GeV in the SPS, and 20 GeV in LEP). Lastly positrons and electrons in LEP are accelerated together to the desired energy, say 46 GeV per beam. The whole sequence takes at least one hour. As soon as the beams are stable, the superconducting quadrupoles at each interaction

region are turned on: they reduce the transverse dimensions of each beam to about 300 μm $\times$ 20 μm r.m.s. The bunches are also squeezed in length to about $\sigma_z = 13$ mm ($4\sigma_z = 5$ cm total). When various sets of collimators are positioned, LEP is ready for physics. The initial luminosity has increased steadily to about 2×10^{31} cm^{-2}s^{-1}. After about 12 hours, when the luminosity has reduced to about one quarter of this value, the beams are dumped and the whole operation is repeated.

Each of the four LEP experiments (ALEPH, DELPHI, L3, OPAL) consists of several "independent" detectors, whose combined role is to measure, with high precision, the energy, direction, charge, and type of the particles produced. Apart from neutrinos, no particle should be able to escape from the detector without leaving some sign of its passage. A solenoid magnet deflects the charged particles so that their electric charge and momentum can be derived from their measured curved trajectories. The interaction region is surrounded by detectors mounted in sequence, all with a cylindrical structure, with a "barrel" and two "end-caps" and 4π coverage. Tracking is performed by a central detector, whilst electron and photon energy measurements are carried out by a high-resolution electromagnetic calorimeter; the magnet iron yoke is instrumented like a hadron calorimeter; a muon detector completes the sequence. A forward detector completes the e.m. coverage by tagging small-angle electrons and photons, and is used as a luminosity monitor. In order to select and measure the cross-section for a specific channel, one needs: (i) a trigger, (ii) the required events (N_i), (iii) the computation of the global efficiency (ϵ_i), and (iv) a luminosity determination ($\int \mathcal{L}\, dt$): $\sigma_i = N_i/(\epsilon_i \int \mathcal{L}\, dt)$.

3.2. Electroweak parameters

At energies of around the Z^0 peak the basic processes are (see Fig. 2)

$$e^+e^- \to Z^0, \gamma \to f\bar{f} , \qquad f\bar{f} = q\bar{q}, \ell\bar{\ell}, \tag{1}$$

where $q\bar{q}$ pairs are $u\bar{u}$, $d\bar{d}$, $s\bar{s}$, $c\bar{c}$, and $b\bar{b}$ ($t\bar{t}$ has a higher mass). Each quark or antiquark hadronizes in a jet of hadrons. Therefore the $q\bar{q}$ pairs are characterized by two opposite jets of hadrons. The quark (or the antiquark) may radiate a gluon, which gives rise to a third jet, see Fig. 3. The $\ell\bar{\ell}$ pairs are either charged (e^+e^-, $\mu^+\mu^-$, $\tau^+\tau^-$) or neutral ($\nu_e\bar{\nu}_e$, $\nu_\mu\bar{\nu}_\mu$, $\nu_\tau\bar{\nu}_\tau$).

A fourth family of quarks and leptons with masses less than half the Z^0 mass would increase the number of open channels, increasing the width of the Z^0 and lowering the height of the peak cross-section. New physics (such as supersymmetric particles) may contribute a fraction of the width contributed by each of the three known families.

Scans around the Z^0 mass were performed, taking data at seven to eleven energies between 88 and 94 GeV. Most of the data points have been measured many times. The behaviour of the cross-section around the Z^0 peak is typical of a resonant state

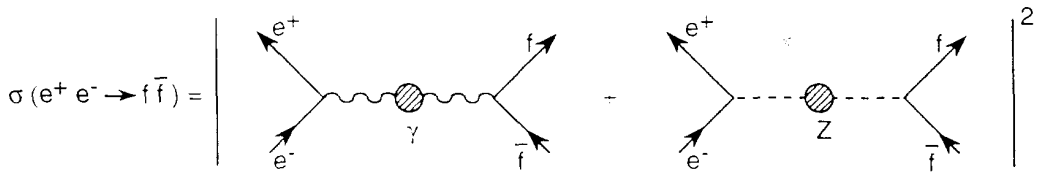

Fig. 2. The basic processes for the cross section $\sigma(e^+e^- \to f\bar{f})$. The bubble in the γ and Z propagators signifies higher order corrections.

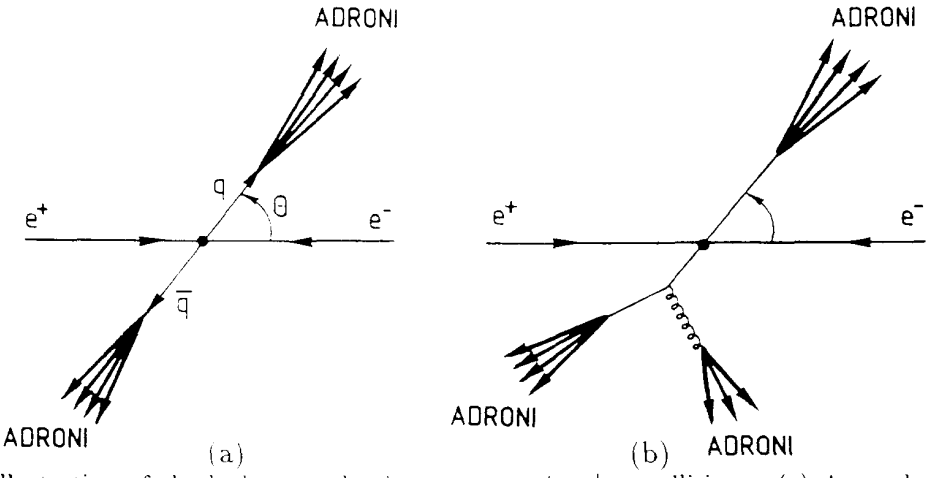

Fig. 3. Illustration of the hadron production processes in e^+e^- collisions. (a) A quark and an antiquark are produced; they then hadronize, leading to a two–jet event. (b) The antiquark emits a gluon; then the quark, the antiquark and the gluon hadronize, leading to a three–jet event.

(see Fig. 4) with $J = 1$ and is well described by a Breit–Wigner formula with an s-dependent width. In fact in the case of γ, Z^0 exchange one has

$$\sigma(e^+e^- \to f\bar{f}) = \underbrace{\tfrac{4}{3}\pi\frac{\alpha(m_Z^2)}{s}}_{\text{electr. term}} + \underbrace{I\frac{s-m_Z^2}{s}}_{\text{interf. term}} + \underbrace{\frac{12\pi}{m_Z^2}\frac{s}{(s-m_Z^2)^2+\frac{s^2}{m_Z^2}\Gamma_Z^2}\Gamma_{e^+e^-}\Gamma_{f\bar{f}}}_{\text{resonant term}} \qquad (2)$$

This formula has to be convoluted with initial state radiation

$$\sigma(s) = \int dz\ \sigma(z,s)G(z). \qquad (3)$$

The first two terms of Eq. 2 may be considered to be small corrections to the main term, which is the Z^0 Breit–Wigner. $\Gamma_{f\bar{f}}$ is the partial width for the decay of the Z^0 into a fermion–antifermion pair, $Z^0 \to f\bar{f}$. The total width Γ_Z is given by

$$\Gamma_Z = \Gamma_h + \Gamma_e + \Gamma_\mu + \Gamma_\tau + N_\nu\Gamma_\nu = \Gamma_{\text{vis}} + \Gamma_{\text{inv}}\ , \qquad (4)$$

where $\Gamma_{\rm h}$ is the total hadronic width and $\Gamma_e, \Gamma_\mu, \Gamma_\tau, \Gamma_\nu$ are the leptonic widths; it is now costumary to use $R_e = \Gamma_{\rm h}/\Gamma_e$, $R_\mu = \Gamma_{\rm h}/\Gamma_\mu$ and $R_\tau = \Gamma_{\rm h}/\Gamma_\tau$. In the Standard Model

$$\left\{ \begin{array}{lcl} \Gamma_{\rm h} & = & \Gamma_{\rm u} + \Gamma_{\rm d} + \Gamma_{\rm s} + \Gamma_{\rm c} + \Gamma_{\rm b} = 1734 \text{ MeV} \\ \Gamma_{\rm u} & = & \Gamma_{\rm c} = 300 \text{ MeV} \quad . \quad \Gamma_{\rm d} = \Gamma_{\rm s} = \Gamma_{\rm b} = 380 \text{ MeV} \\ \Gamma_e & = & \Gamma_\mu = \Gamma_\tau = 83.4 \text{ MeV} \\ \Gamma_\nu & = & 166.5 \text{ MeV} \quad , \quad N_\nu = 3 \quad . \quad \Gamma_{\rm inv} = 499 \text{ MeV} \\ \Gamma_{\rm Z} & = & \Gamma_{\rm h} + 3\Gamma_\ell + 3\Gamma_\nu = 2487 \text{ MeV} \; . \end{array} \right. \tag{5}$$

At $s = m_Z^2$, the resonant part of Eq. 2 yields

$$\sigma(s = m_Z^2) = \frac{12\pi(\hbar c)^2}{m_Z^2} \; \frac{\Gamma_e \Gamma_f}{\Gamma_Z^2} \; . \tag{6}$$

For $e^+e^- \rightarrow Z \rightarrow$ hadrons, the resonant part of Eq. 2 gives

$$\sigma_{\rm h}(s) = \sigma_{\rm h}^p \frac{s\Gamma_Z^2}{(s - m_Z^2)^2 + s^2\Gamma_Z^2/m_Z^2} \; , \tag{7}$$

where $\sigma_{\rm h}^p$ is the pole hadron cross-section:

$$\sigma_{\rm h}^p = \frac{12\pi(\hbar c)^2 \Gamma_e \Gamma_{\rm h}}{m_Z^2 \Gamma_Z^2} \; . \tag{8}$$

In the electroweak theory the partial width Γ_f may be expressed in terms of vector (g_v) and axial-vector (g_a) coupling constants:

$$g_a = I_{3\rm f} \quad , \quad g_v = I_{3\rm f} - 2Q_{\rm f} \sin^2\theta_{\rm w} \; , \tag{9}$$

where $I_{3\rm f}$ is the third component of the weak isospin, $Q_{\rm f}$ is the electric charge of the fermion and $\theta_{\rm w}$ is the weak mixing angle. At the lowest order (tree level) one has

$$\Gamma_f = N_{\rm c} \frac{G_\mu \, m_Z^3}{6\pi\sqrt{2}} (g_v^2 + g_a^2)(1 - \delta_f^{\rm QED}) \tag{10}$$

where $N_{\rm c}$ is the number of colours ($N_{\rm c} = 1$ for leptons, $N_{\rm c} = 3$ for quarks), $\delta_f^{\rm QED} = 3q_f^2\alpha(m_Z^2)/4\pi$ accounts for final state photonic corrections. The angular distributions of the produced $f\bar{f}$ exhibit asymmetries, which at m_Z may be written as

$$A_{\rm FB}^{0,f} = \frac{3}{4} A_e A_f \quad , \quad A_f = \frac{2g_v g_a}{g_v^2 + g_a^2} \; . \tag{11}$$

At each energy, measurements of the cross-sections have been carried out for $Z^0 \rightarrow$ hadrons, $Z^0 \rightarrow e^+e^-$, $Z^0 \rightarrow \mu^+\mu^-$, $Z^0 \rightarrow \tau^+\tau^-$, the forward-backward lepton asymmetries $A_{\rm FB}^{\rm e}$, $A_{\rm FB}^{\mu}$, $A_{\rm FB}^{\tau}$, the τ polarization asymmetry P_τ, the $b\bar{b}$ and $c\bar{c}$ partial widths and forward-backward asymmetries, and the $q\bar{q}$ charge asymmetry.

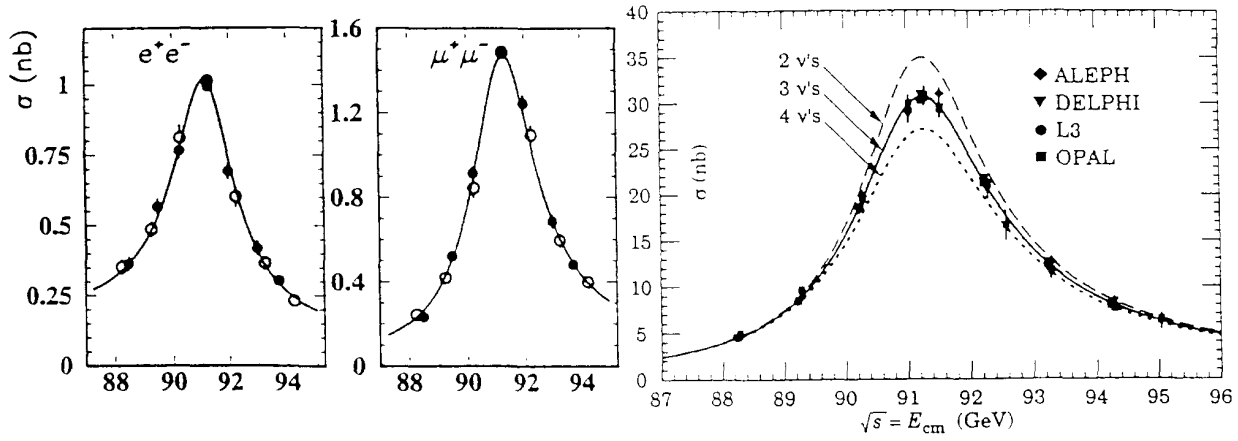

(a) (b)

Fig. 4. (a) The measured cross-sections for $e^+e^- \to e^+e^-$ (for $|\cos\theta| < 0.7$) and $e^+e^- \to \mu^+\mu^-$. The lines are the results of the fits to all the data. (b) Measured hadron data compared with the predictions of the Standard Model for two, three and four generations [2].

Each experiment performs fits and obtains nine parameters (m_Z, Γ_Z, σ_h^p, Γ_e, Γ_μ, Γ_τ, A_{FB}^e, A_{FB}^μ, A_{FB}^τ). One checks that $\Gamma_e = \Gamma_\mu = \Gamma_\tau$ and $A_{FB}^e = A_{FB}^\mu = A_{FB}^\tau$ (lepton universality). The fit is then repeated with five parameters (m_Z, Γ_Z, σ_h^p, Γ_ℓ, A_{FB}^ℓ).

In order to combine results from the four experiments at LEP, each experiment provides a set of 9 optimized parameters (five parameters only if lepton universality is assumed). These parameters are optimized assuming a common systematic error. The present results, using lepton universality, are shown in Table 2 [1].

From the results given in Table 2 and from the results obtained at SLD, at the Fermilab $p\bar{p}$ collider and from ν-experiments, can be calculated the electroweak parameters given in Table 3. Note the precise value of the number of light neutrino families N_ν and of the strong coupling constant α_s at m_Z. Note also that the value of m_t obtained "below threshold" is in very good agreement with the directly measured value. By feeding in the measured value of m_t one obtains the χ^2 curve of Fig. 5 for the Higgs mass: the graph is suggestive of a small m_H. It is possible that with the new 1995 scan around the Z^0 at LEP, together with a more precise determination of m_t and m_W and a better knowledge of all the parameters, a better determination of m_H below threshold could be achieved.

The asymmetry measurements at LEP can be combined into a single observable, the effective electroweak mixing angle ($\sin^2\theta_{eff}^\ell$), which may be defined in several ways. The LEP collaborations use

$$\sin^2\theta_{eff}^\ell = \frac{1}{4}\left(1 - \frac{g_v}{g_a}\right) . \qquad (12)$$

Table 2. Average electroweak parameters from the results of the four LEP experiments, assuming lepton universality [1].

Parameter	Average LEP	Standard Model
m_Z	91188.4 ± 2.2 MeV	-
Γ_Z	2496.3 ± 3.2 MeV	2497
σ_h^p	41.488 ± 0.078 nb	41.45
$R_\ell = \Gamma_h/\Gamma_\ell$	20.788 ± 0.032	20.773
A_{FB}^ℓ	0.0172 ± 0.0012	0.0159
Γ_ℓ	83.93 ± 0.14 MeV	83.4
Γ_h	1744.8 ± 3.0 MeV	
Γ_{inv}	499.9 ± 2.5 MeV	499
$A_\tau = -P_\tau$	0.1418 ± 0.0075	0.1455
A_e	0.1390 ± 0.0089	0.1455
R_b	0.2219 ± 0.0017	0.2156
R_c	0.1543 ± 0.0074	0.1724
$BR_\ell = \Gamma_\ell/\Gamma_Z$	3.36 %	
BR_h	69.9 %	
BR_{inv}	20.0 %	

Table 3. Results of the analyses based on the LEP data, the SLD measurements, the m_W measurements at Fermilab and N_ν measurements. The second errors in m_t and α_s correspond to the variation of the central value when varying the Higgs mass in the interval $60 < m_H < 1000$ GeV [1].

g_v^ℓ	-0.03797 ± 0.00071
g_a^ℓ	-0.50111 ± 0.00041
$N_\nu = \Gamma_{inv}/\Gamma_\nu^{SM}$	2.991 ± 0.016
m_t (GeV)	$178 \pm 8^{+17}_{-20}$
$\alpha_s(m_Z)$	$0.123 \pm 0.004 \pm 0.002$
$\sin^2\theta_{eff}^\ell$	$0.23172 \pm 0.00024^{+0.00007}_{-0.00014}$
$1 - m_W^2/m_Z^2$	$0.2237 \pm 0.0009^{+0.0004}_{-0.0002}$
m_W (GeV)	$80.346 \pm 0.046^{+0.012}_{-0.021}$

A precise determination of this parameter is given in Table 3.

3.3. Multihadronic events

Multihadronic production in e^+e^- annihilations is thought to proceed via four distinct phases as illustrated in Fig. 6 [2].

i) In the first phase the initial e^+e^- pair annihilates into a virtual Z^0/γ, which decays into the primary $q\bar{q}$ pair. Before e^+e^- annihilation, a bremsstrahlung γ may be emitted by the initial electron or positron; this reduces the effective total c.m. energy. The production of the primary $q\bar{q}$ pair is well described by the electroweak perturbative theory and it occurs at a scale of distances of the order of 10^{-17} cm.

ii) In the second phase the quark q or the antiquark $\bar{q}$ may radiate a gluon, which may

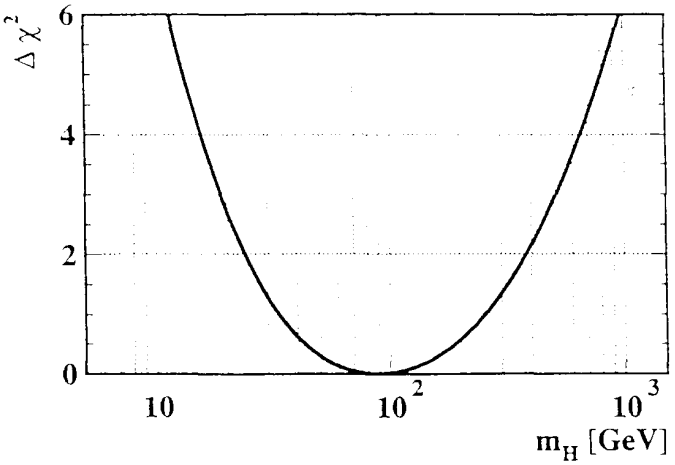

Fig. 5. The $\Delta\chi^2$ for the fit of the electroweak precision measurements versus m_H [1].

subsequently radiate a second gluon (forming a three-gluon vertex), or may radiate a $q\bar{q}$ pair. This phase is described by perturbative QCD and occurs over distances of about 10^{-15} cm.

iii) In the third phase the coloured partons, i.e. quarks and gluons, fragment (hadronize) into colourless hadrons. This process cannot be analysed with perturbative methods; in the absence of an exact theory it has to be treated with models. Hadronization occurs over distances of the order of 1 fm.

iv) In the fourth phase the produced hadron resonances decay quickly via strong interaction into stable hadrons (e.g. $\rho^0 \to \pi^+\pi^-$); other hadrons decay via the electromagnetic interaction ($\Sigma^0 \to \Lambda^0\gamma$, $\pi^0 \to \gamma\gamma$). A few (like the b-hadrons) decay via weak interaction with lifetimes of the order of 10^{-12} s. This phase is described by models which include the experimental information on lifetimes and branching ratios.

The perturbative phase (ii) is often analysed with "matrix elements" computed via Feynman diagrams up to the second order in α_s (at this order only four partons may be generated). The second method used is called "hadron cascade" or "parton shower"; it is based on a sum of logarithmic terms in all orders of perturbation theory (next to leading order: at LEP energy it generates up to ten partons).

The phase (iii) is modelled with string fragmentation or cluster fragmentation.

Fig. 7 shows the average charged multiplicity in e^+e^- collisions plotted versus c.m. energy. At the Z^0 peak the average charged multiplicity is $\langle n \rangle = 20.8 \pm 0.2$.

A number of shape parameters (Sphericity, Aplanarity, Thrust,...) have been introduced to characterize the global event structure of multihadronic final states. Their studies provide checks of QCD and allow optimization of the Monte Carlos used. A major role is played by the Monte Carlos used for corrections and analyses. It is important that they are optimized to the measured experimental distributions defined above. For each track k of a multihadronic event, we define the rapidity, the transverse and longitudinal momenta and the variable $x_k = p_k / E_{\text{beam}}$.

Within the framework of QCD, the standard process is the decay $Z \to q + \bar{q}$

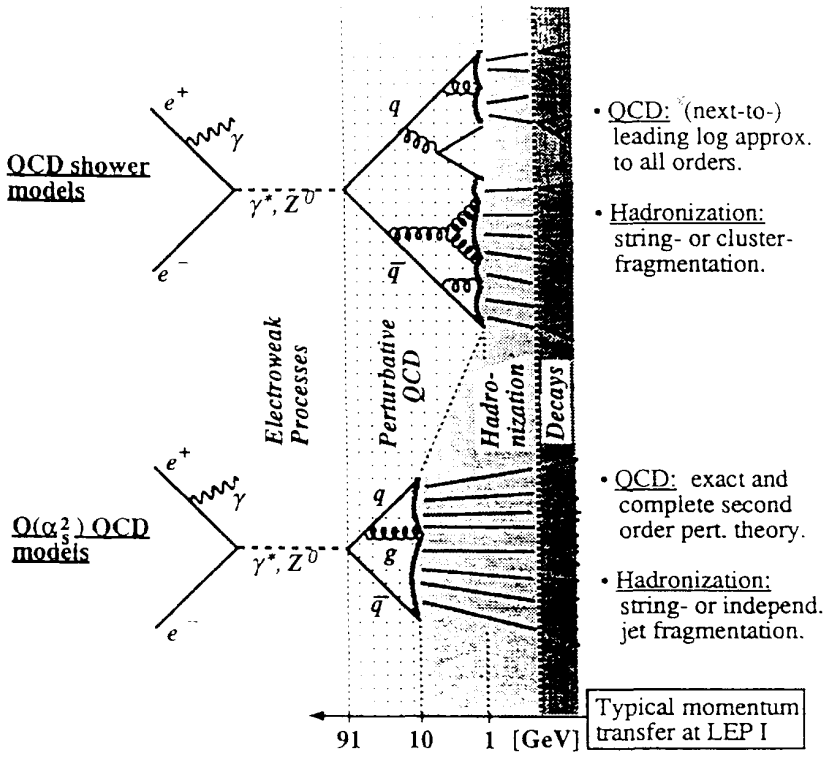

Fig. 6. Model of multihadronic production in e^+e^- collisions.

with subsequent $q \rightarrow$ jet-1 and $\bar{q} \rightarrow$ jet-2. The quark or the antiquark may emit a gluon, thus leading to a three-jet event. The relative production rates of multijet events are determined by the value of the strong coupling constant α_s. According to the hypothesis of asymptotic freedom, α_s is expected to decrease with increasing energy. The gluon is emitted by a process similar to bremsstrahlung: the number of low-energy gluons, and thus the number of low-energy jets, is considerably larger than the number of high-energy ones. For low-energy gluons the three-jet structure may be experimentally difficult to observe and has to be established by an empirical procedure (for instance the Jade algorithm).

The strong coupling constant $\alpha_s(\mu)$ can be written as a function of $\ln(\mu^2/\Lambda^2)$, where Λ is the QCD scale parameter and μ is the QCD renormalization scale

$$\alpha_s(\mu) = \frac{12\pi}{(33-2n_f)\,\ln(\mu^2/\Lambda^2)}\left[1 - \frac{6(153-19n_f)}{(33-2n_f)^2}\,\frac{\ln[\ln(\mu^2/\Lambda^2)]}{\ln(\mu^2/\Lambda^2)}\right] + \ldots , \qquad (13)$$

where n_f, the number of quarks with mass smaller than the energy scale μ, is taken to be equal to 5. Equation 13 predicts $\alpha_s \rightarrow 0$ as $\mu \rightarrow \infty$ (asymptotic freedom property). LEP provided the first complete experimental evidence for the running of α_s, see Fig. 8. With increasing energy, n_f and the terms that depend on n_f change by discrete amounts as a new flavour threshold is crossed. If Eq. 13 should be valid for all values of μ, then Λ must also change discretely through a flavour threshold. This

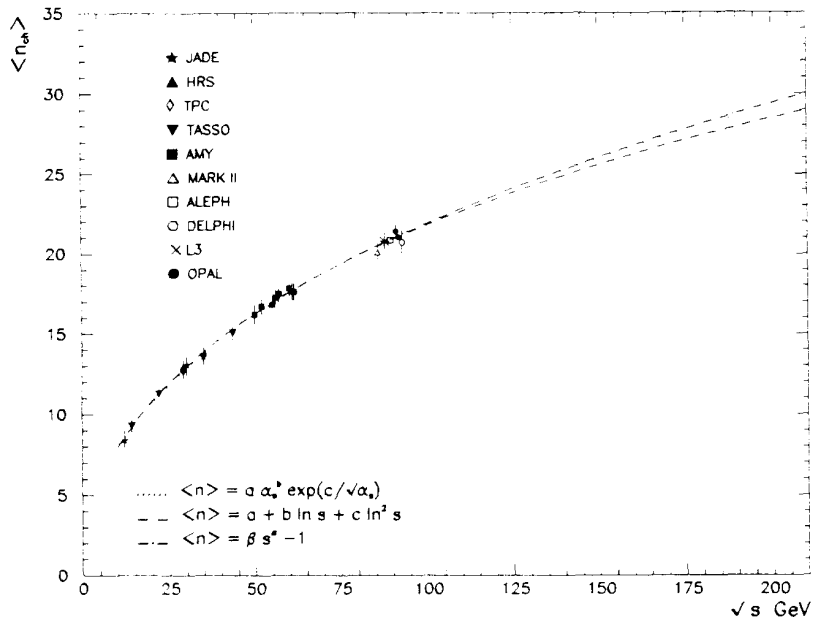

Fig. 7. Average charged multiplicity in e^+e^- collisions plotted versus c.m. energy.

implies a different value of Λ for each range of μ corresponding to an effective number of massless quarks: $\Lambda \to \Lambda(n_f)$. The renormalization scale μ^2 is usually chosen to be the global centre-of-mass energy ($\mu^2 = E_{\rm cm}^2$). A definition $\mu^2 = f \cdot E_{\rm cm}^2$, with $0.001 < f < 0.01$, results in a better description of the jet production rates.

The coupling constant of the strong interaction, α_s, is a fundamental parameter which may be determined from many types of measurements: (i) from event topology (shape variables), (ii) from $\Gamma_{\rm h}/\Gamma_\ell = R_Z^0(1 + \delta_{\rm QCD})$. All LEP experiments checked the flavour independence of α_s and the decrease of α_s with increasing energy.

3.4. Quark and gluon jet differences

We shall discuss in more detail the differences between hadron jets started by a quark and by a gluon. QCD predicts different coupling strengths for the radiation of an additional gluon from either a quark or a gluon. These coupling strengths are governed by the colour factors for gluon emission, which have the values $C_F = 4/3$ and $C_A = 3$ for radiation from a quark and a gluon, respectively. These are inclusive factors which need corrections to predict real jets. QCD predicts that a gluon is more likely to radiate a gluon than a quark. It is expected that a gluon jet will have a higher particle multiplicity, a softer particle spectrum and will be broader than a quark jet of equal energy [3].

Experimental tests of these predictions have been made using three-jet multi-hadron events in symmetric configurations. In the LEP experiments, a jet-finding

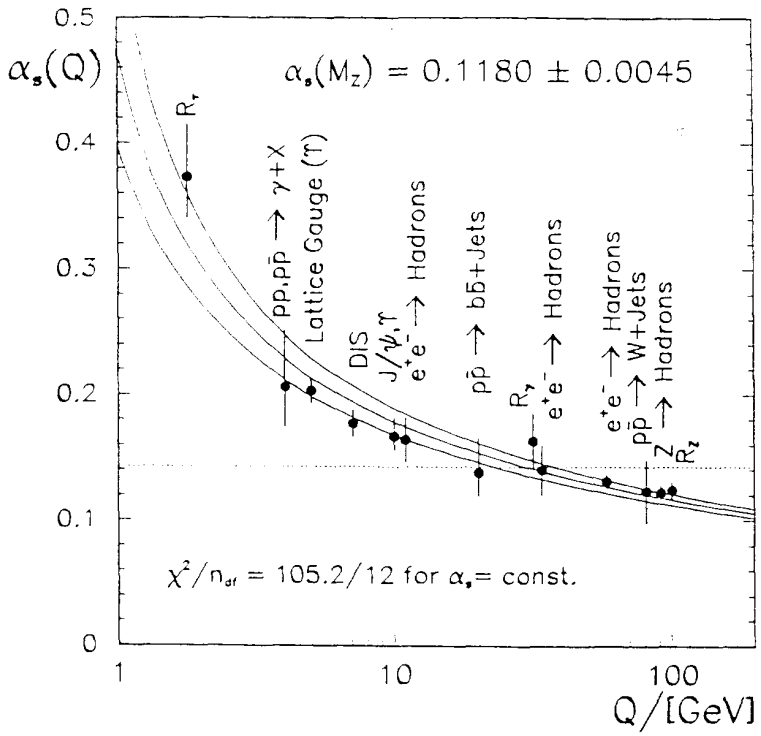

Fig. 8. A summary of measurements of α_s, compared with QCD expectations for $\alpha_s(m_Z) = 0.1180 \pm 0.0045$ and $N_f = 5$ flavours.

algorithm is applied to the multihadronic events, and those events in which three jets are reconstructed are retained. Furthermore, events are only retained if two jets form angles of $(150 \pm 10)^\circ$ to the third jet (Fig. 9a). This requirement gives a configuration in which two jets have approximately equal energies and the third jet has a significantly higher energy. The highest energy jet is a quark jet while the two lower energy jets are composed of a roughly equal mixture of quark and gluon jets. Using microvertex detectors, a subsample of the symmetric events is selected, in which one of the two lower energy jets contains a secondary vertex which signals a b–quark decay. Since b–quarks are almost entirely produced at the electroweak vertex, the presence of such a decay indicates that the tagged jet is very likely a b–quark jet. The remaining lower–energy jet is then a gluon jet. Only these anti–tagged gluon jets are considered further here (the tagged quark jets are biased and therefore are not used).

The heavy–flavour tagging allows gluon jets to be identified with a purity of about 93%; it is then possible to construct the distribution of interest, e.g. the fragmentation function for the two samples separately. Denoting the distribution for all lower–energy jets as D_{all} and that for the gluon jets in the tagged sample as D_{tag}, two equations can be written: $D_{\mathrm{all}} = 0.49 \cdot G + 0.51 \cdot Q$, $D_{\mathrm{tag}} = 0.93 \cdot G + 0.07 \cdot Q$, where G and Q are the fragmentation function distributions for pure gluon and quark jets, respectively; the coefficients correspond to the jet purity. The linear equations can be solved for the pure jet properties. Since the jets have been selected from events with symmetric topologies, the quark and gluon jets have equal energies and identical jet

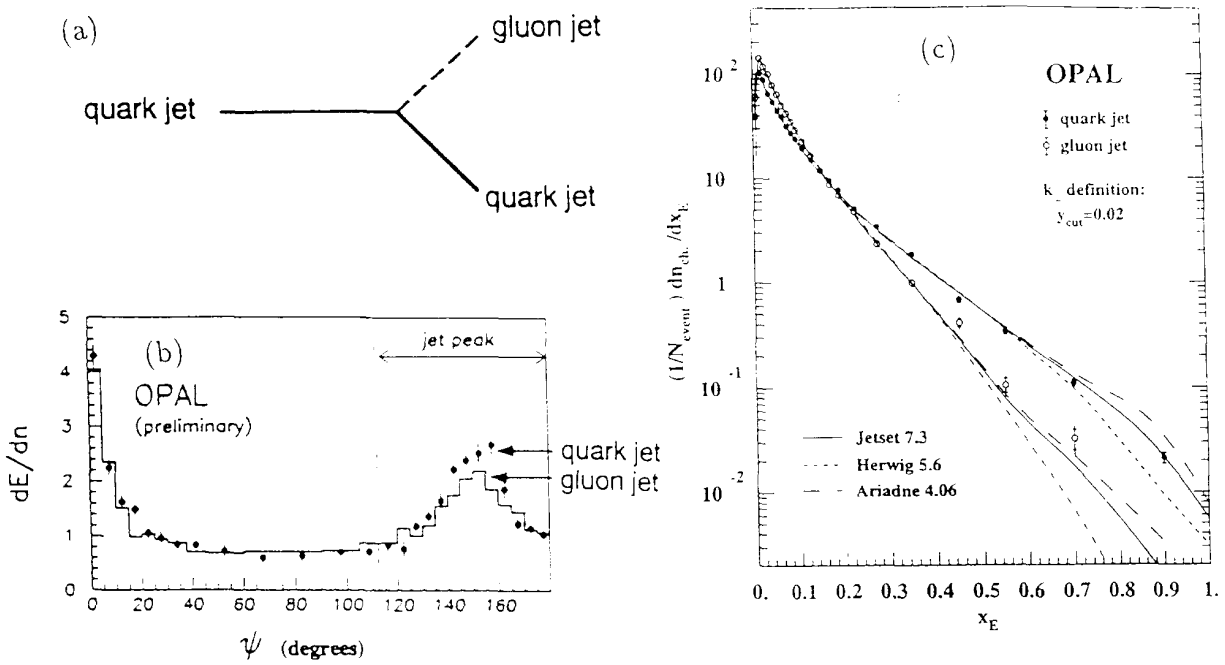

Fig. 9. (a) The chosen symmetric topology to study quark gluon jet differences; (b) the angular distribution of jet energy and (c) the charged particle fragmentation functions.

environments, thus facilitating the comparison of jet properties.

Fig. 9c shows the fragmentation function, measured as a function of the quantity $x_E = E/E^{jet}$, which is the scaled energy of a hadron with respect to the energy of the jet to which it is assigned. Gluon jets (open points) have fewer particles with large energies and more particles with low energies, and hence the particle energy spectrum is softer for gluon jets than for quark jets.

The angular spread of a jet may be studied by measuring the fraction of the jet energy contained in annular rings coaxial with the jet. This distribution is shown in Fig. 9b. Once again, clear differences between quark and gluon jet properties are seen. The gluon jets have more of their energy distributed at large angles to the jet axis, and therefore can be considered to be broader than the quark jets.

To leading order, the QCD prediction for the ratio of gluon to quark jet multiplicities is $[\langle n\rangle_g/\langle n\rangle_q] = C_A/C_F = 9/4$, which becomes slightly smaller ($\simeq 2$) in next-to-next-leading order. However, this prediction refers to the production of $q\bar{q}$ or gg in a colour singlet state at asymptotically high energies, and therefore may not be directly comparable with the experimental measurements at finite centre-of-mass energies. The measurements of charged particle multiplicities in symmetric 150° configurations vary between $\langle n^{\rm ch}\rangle_g/\langle n^{\rm ch}\rangle_q = 1.23$ and 1.11 according to which jet algorithm is used.

We conclude that the measurements at LEP have confirmed that gluon jets have softer particle spectra, higher multiplicities, and are broader than quark jets of the

same energy.

4. Physics below threshold

Because of radiative corrections, the LEP precision measurements are sensitive to contributions from the top quark and from the Higgs boson. The contributions depend on the masses m_t and m_H. Using the data up to 1994, the measurements predicted $m_t = 173\ ^{+12}_{-13}\ ^{+18}_{-20}$ GeV, where the second error is mainly due to the uncertainty in m_H. With SLD measurements of A_{LR}, slightly larger values are preferred. The final value is in perfect agreement with the measured value at Fermilab. Checks were also made that the b-quark has $I = \frac{1}{2}$ and $I_3 = -\frac{1}{2}$, which require a t-quark with $I_3 = +\frac{1}{2}$.

The dependence on m_H is weaker than on m_t. Nevertheless, by fixing m_t at the Fermilab measured value and using all available information on m_W a first estimate of m_H has been obtained, see Fig. 5. The predicted value is low, around 80 GeV, but with a large uncertainty.

Several authors pointed out the importance of precision measurements capable of yielding information below threshold, as has already proved valuable for $W^{\pm}$, Z^0 and t. It may be that, for a long time, precision measurements will be the only source of information for particles with very large masses.

5. The Left-Right Asymmetry at SLAC

In the electroweak part of the Standard Model, the two helicity states of a particle with mass are considered as two distinct particles: they have different quantum numbers, different weak charges and different interactions. It is important to check these properties and to make use of them to measure with high precision $\sin^2\theta_W$.

The SLAC linear collider achieved collisions between partially longitudinally-polarized electrons and unpolarized positrons. One can measure the Left-Right Asymmetry

$$A_{LR} = \frac{1}{P_e}\frac{N_L(e_L^- + e^+ \to Z) - N_R(e_R^- + e^+ \to Z)}{N_L(e_L^- + e^+ \to Z) + N_R(e_R^- + e^+ \to Z)}\ , \tag{14}$$

where $N_L(e_L^- + e^+ \to Z)$ is the number of events for left-handed electrons, yielding the process $e_L^- + e^+ \to Z \to f + \overline{f}$ (where $f + \overline{f}$ can be any quark and any charged lepton, excluding the e^+e^- final state for which the γ-exchange t-channel could contribute). Similarly $N_R(e_R^- + e^+ \to Z)$ is the number of events for the right-handed electrons; P_e is the average electron polarization ($\sim 63\%$ in 1993, $\sim 80\%$ in 1994). In the SM the A_{LR} parameter is given by

$$A_{LR} = \frac{(g_L^l)^2 - (g_R^l)^2}{(g_L^l)^2 + (g_R^l)^2} = \frac{2(1 - 4\sin^2\theta_W)}{1 + (1 - 4\sin^2\theta_W)^2}\ . \tag{15}$$

Thus a measurement of A_{LR} yields a precise measurement of $\sin^2\theta_W$. Using their 1993

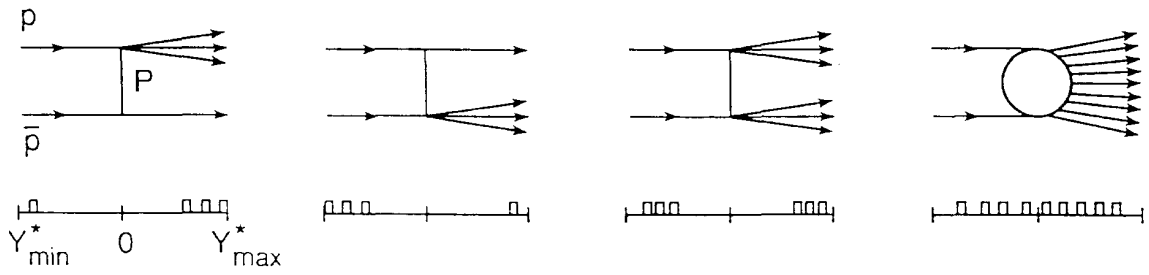

(a) (b) (c) (d)

Fig. 10. Pictorial descriptions of production processes with characteristic rapidity distributions. P indicates Pomeron exchange, that is the exchange of the highest Regge trajectory with the quantum numbers of the vacuum. (a) Fragmentation of the beam particle a. (b) Fragmentation of the target b. (c) Double fragmentation of a and b. (d) central collision production reaction.

data based on about 50000 Z^0, the SLAC measurement of $A_{LR} = 0.1637 \pm 0.0075$ yields $\sin^2\theta_W = 0.2294 \pm 0.0010$ [4].

6. FERMILAB results

6.1. Elastic and total cross-sections

The total $p\bar{p}$ cross-section may be written as

$$\sigma_{tot} = \sigma_{el} + \sigma_{inel} = \sigma_{el} + \sigma_{sd} + \overline{\sigma}_{sd} + \sigma_{dd} + \sigma_{nd} \ , \tag{16}$$

where σ_{el} is the elastic cross-section, σ_{sd} is the single diffractive cross-section when the incoming proton fragments into a number of particles, $\overline{\sigma}_{sd}$ is the single diffractive cross-section for the fragmentation of the antiproton (at high energies $\sigma_{sd} = \overline{\sigma}_{sd}$), σ_{dd} is the double diffractive cross-section, σ_{nd} is the non-diffractive part of the inelastic cross-section (Fig. 10).

The elastic, single diffractive and double diffractive processes give rise to low multiplicity events with particles emitted in the very forward and very backward regions in the c.m. system. The single diffractive cross-section seems to increase slowly from 6 mb to about 9 mb in the range $20 < \sqrt{s} < 1800$ GeV. The non-diffractive cross-section is the main part of the inelastic cross-section; the non-diffractive processes give rise to high multiplicity events and to particles emitted at all angles. Most of the non-diffractive cross-section concerns particles emitted with low transverse momentum (low p_t physics) with properties which change slowly with c.m. energy ($\ln s$ physics). A relatively small part of the non-diffractive cross-section is due to central collisions among the colliding particles and gives rise to high p_t jets of particles emitted at relatively large angles (large p_t physics). The contribution of jet physics increases with c.m. energy.

The behaviour of the $\bar{p}p$, pp, π^-p, π^+p, K^-p and K^+p cross-sections versus energy for c.m. energies between 3 and 70 GeV is summarized in Fig. 11: as the

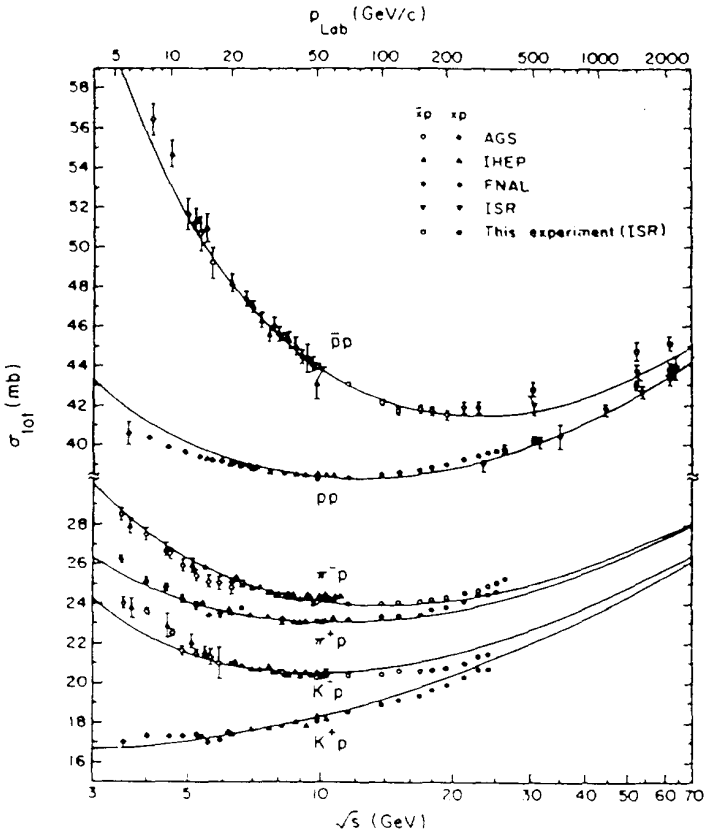

Fig. 11. Total cross-sections for high-energy hadron-hadron scattering. The curves are computed according to Lipkin's parametrization.

energy increases, the first five cross-sections decrease, reach a minimum and then increase. The K^+p cross-section increases in this entire energy range: its rise was already evident and established at Serpukhov energies [5]. All the differences $[\sigma_{\rm tot}(\bar{x}{\rm p}) - \sigma_{\rm tot}(x{\rm p})]$ decrease with increasing energy.

Fig. 12 shows a compilation of $\bar{\rm p}$p and pp total cross-sections, including Tevatron and cosmic ray measurements [5–7]. The data are well described by the empirical fit of Amaldi et al., repeated recently by Augier et al. [6]. They fitted the high-energy data of $\sigma_{\rm tot}$ and ρ for pp and $\bar{\rm p}$p scattering using once subtracted dispersion relations for odd and even under crossing forward amplitudes, assuming that the odd part becomes negligible at very high energies. They used the following parametration

$$\sigma_{\pm}(E) = A_1 E^{-N_1} \mp A_2 E^{-N_2} + \sigma_\infty \tag{17}$$

where

$$\sigma_\infty = C_0 + C_2 \left[\ln\,(s/s_0)\right]^\gamma \quad , \quad s_0 = 1\ {\rm GeV}^2 \tag{18}$$
$$C_0 = 30\ ^{+3}_{-4} \quad , \quad C_2 = 0.10\ ^{+0.15}_{-0.06} \quad , \quad \gamma = 2.25\ ^{+0.35}_{-0.31}.$$

The terms $A_1 E^{-N_1}$ and $A_2 E^{-N_2}$ are Regge type terms which describe the behaviour at relatively low energies and the difference between $\sigma_{\rm tot}(\bar{\rm p}{\rm p})$ and $\sigma_{\rm tot}({\rm pp})$. E is

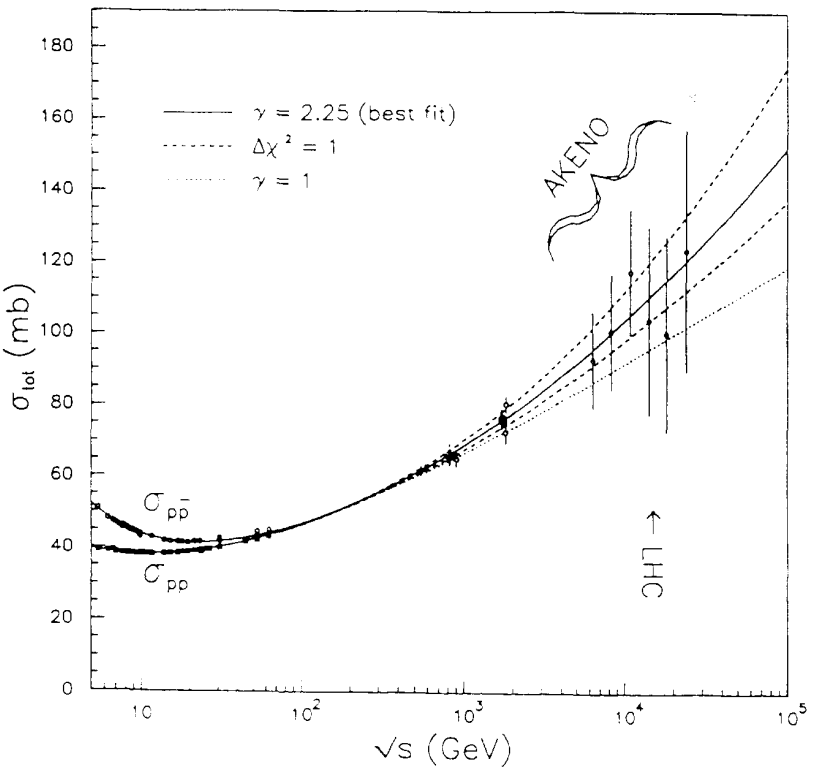

Fig. 12. Compilation of $\bar{p}p$ and pp total cross-sections including cosmic ray measurements. The solid line is a fit of the σ_{tot} and ρ data with dispersion relations [5-8]; the region of uncertainty is delimited by dashed lines.

the energy of the incoming particle in the lab system. Notice the approximate $\ln^2 s$ behaviour of the very high-energy σ_{tot}. The fit predicts $\sigma_{tot} = (111 \pm 8)$ mb and $\rho = 0.133 \pm 0.018$ for pp scattering at $\sqrt{s} = 16$ TeV.

Successful fits to σ_{tot}, ρ and b have also been done by M. Block et al. [8] in the context of a QCD inspired model and by Donnachie and Landshoff [8].

Detailed analyses of the $\bar{p}p$ elastic scattering data at the highest avaible energies yielded values of the elastic scattering slope b at the average values of $|t| \sim 0.1$ (and ~ 0.2) $(\mathrm{GeV/c})^2$, and of the ρ parameter ($d\sigma/dt = d\sigma(t=0)/dt\ e^{bt}$, $\rho = \mathrm{Re}f(0)/\mathrm{Im}f(0)$). The integration of the elastic differential cross-sections yielded σ_{el} and then the ratios σ_{el}/σ_{tot}. There is reasonable agreement among the data from different experiments, within their relatively large uncertainties.

The slope parameter b for $\bar{p}p$ keeps increasing up to $\sqrt{s} = 1.8$ TeV, at a rate which is probably larger than $\ln s$. The elastic $\bar{p}p$ cross-section continues to rise at a rate close to $\ln^2 s$ or larger. Therefore the ratio σ_{el}/σ_{tot} increases with energy, reaching the value of about 0.24 at $\sqrt{s} = 1.8$ TeV, see Fig. 13. This value is still far below the black disk value of 0.5. However the Fourier transformation of the t-distribution yields a form factor which at $r = 0$ has reached the value of 0.5; this means that the center of the proton has become more opaque, almost black.

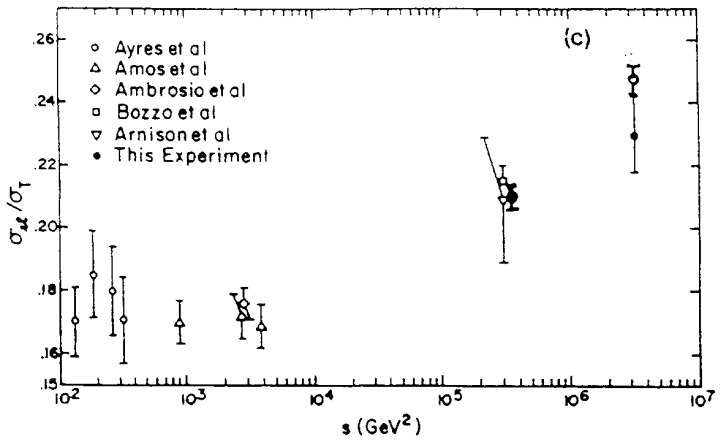

Fig. 13. Ratio of the elastic to total cross-section for $\bar{p}p$ versus s.

Fig. 14 shows the large angle elastic differential cross section at $\sqrt{s}$=1.8 TeV: it is apparent the interest in new measurements of $\bar{p}p$ elastic scattering at $\sqrt{s} = 1.8$ TeV in the $0.5 < |t| < 1$ (GeV/c)^2 region to establish if the dip–bump structure seen at lower energies still exists, and to check if the diffraction pattern has really gone from a shape $\frac{d\sigma}{dt} = Ae^{bt+ct^2}$ with c positive to a shape with $c = 0$. Some models predict that at higher energies the c value should become negative. Thus the diffraction pattern would approach the classical diffraction pattern from a disk of radius R and opacity a, described by a Bessel function of order 1, J_1.

New values of ρ, the ratio of the real to the imaginary part of the $\bar{p}p$ elastic scattering amplitude, were obtained from elastic scattering data in the Coulomb-Nuclear interference region. The new values of ρ, follow the dispersion relation calculations.

In most elastic scattering analyses the polarization effects are neglected, since such effects are thought to decrease as the energy increases; besides they are small in the forward direction. In fact sizable and measurable spin and asymmetry effects have been observed at $p_{\rm lab} = 28$ GeV/c and at high p_t, where the cross section for pp elastic scattering with spins parallel is about four times larger than the cross section for spins antiparallel at $p_t \sim 2-3$ GeV/c [9]. Spin effects need to be investigated more systematically, both experimentally and theoretically.

6.2. Jet production cross-sections

The two–jet production in $\bar{p}p$ collisions, $\bar{p}+p \rightarrow$ 2 jets + X, is due to parton–parton processes. Fig. 15a shows the inclusive jet cross–section measured by the CDF collaboration as function of $E_{T\rm jet}$ up to 400 GeV at $\sqrt{s} = 1800$ GeV [10]. Good agreement is found with the QCD prediction, thus excluding new physics, such as that expected from subconstituent contact interactions.

Fig. 15b shows the polar angular distribution measured by the D0 collaboration [10]. This distribution is sensitive to the type of partons involved. Again good agreement

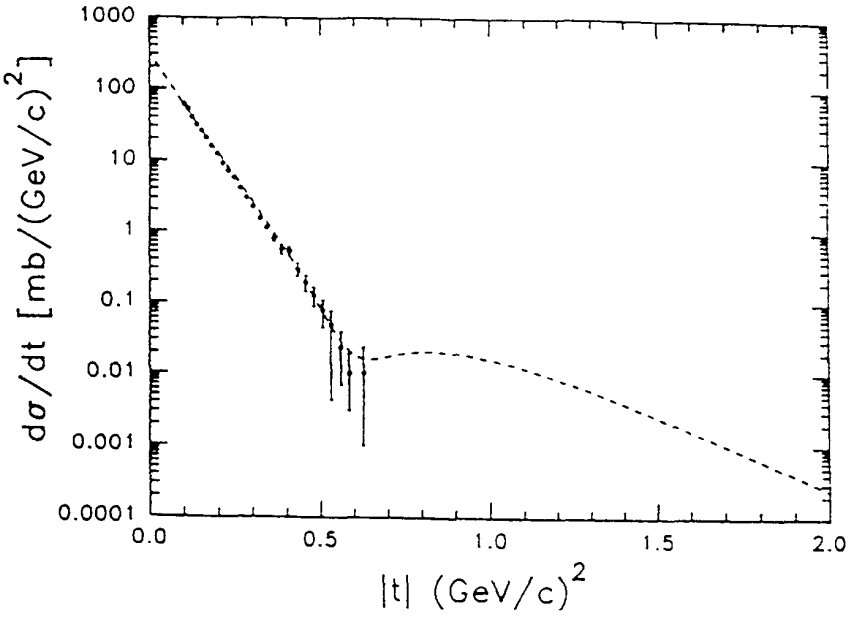

Fig. 14. Differential elastic scattering cross-section for $\bar{p}p$ at $\sqrt{s} = 1.8$ GeV at Fermilab together with a fit by Block et al. [8].

is found with the QCD predictions.

6.3. The top quark

The CDF and D0 collaborations have presented evidence for top-quark production in $p\bar{p}$ collisions at $\sqrt{s} = 1.8$ TeV [11]. According to the SM, in $p\bar{p}$ collisions the dominant modes of top-quark production is via quark-antiquark annihilation or gluon-gluon fusion: $q + \bar{q} \rightarrow t+\bar{t}$, $g + g \rightarrow t+\bar{t}$. The SM cross-sections for these channels are predicted to be around 5–6 pb for $m_t = 170$–180 GeV. The dominant SM decays of the top quark are

$$t \rightarrow W^+ + b \quad , \quad t \rightarrow W^+ + (s \text{ or } d) \quad , \quad t \rightarrow g + W^+ + (b, s \text{ or } d) \qquad (19)$$

and likewise for $\bar{t}$.

The CDF and D0 Collaborations searched for (i) lepton pairs (ee, $\mu\mu$, eμ resulting from the decays of W^+W^-) plus jets (from the decays of b, s, d, g), and (ii) single leptons plus jets. This sample was further divided in b-tagged and untagged channels according to whether or not a charged lepton was found such that b$\rightarrow$ lepton+X.

CDF observed a total of 33 events over a total background of 23 events in a 67 pb^{-1} data sample of $p\bar{p}$ collisions at $\sqrt{s} = 1.8$ TeV. It yielded $m_t = 176 \pm 8(\text{stat}) \pm 10(\text{syst})$ GeV and a $t\bar{t}$ production cross-section of $6.8^{+3.6}_{-2.4}$ pb.

D0 observed 17 events with an expected background of 3.8 events in a 50 pb^{-1}

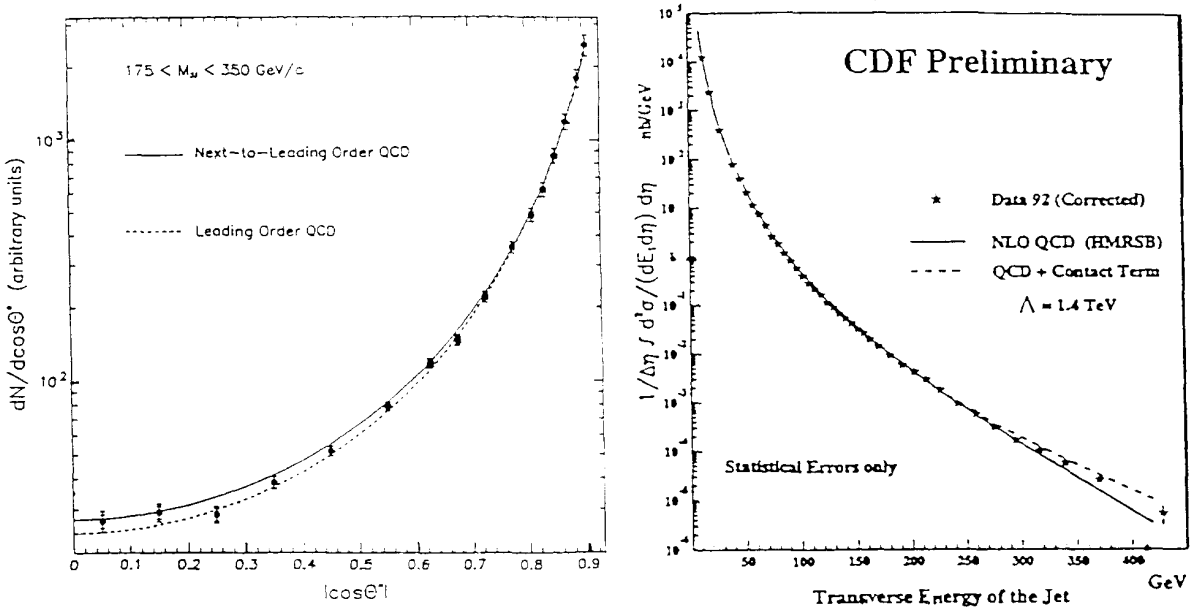

(a) (b)

Fig. 15. (a) Inclusive jet cross-section referred to the $p\bar{p}$ line of flight; (b) angular distribution of parton-parton scattering [10].

data sample. This yielded $m_t = 199^{+19}_{-21}(\text{stat}) \pm 22(\text{syst})$ GeV and $\sigma_{t\bar{t}} = 6.4 \pm 2.2$ pb.

7. HERA results

7.1. Deep inelastic scattering

As already stated, the HERA collider in Hamburg is an asymmetric ep collider,

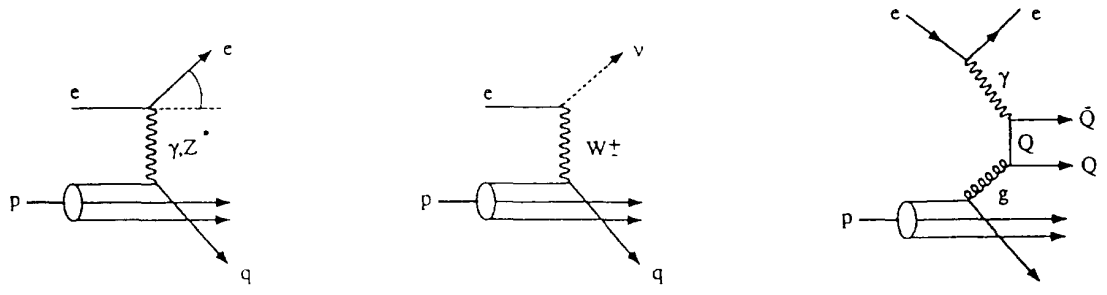

(a) (b) (c)

Fig. 16. The basic processes contributing to deep-inelastic scattering: (a) neutral current scattering, (b) charged current scattering and (c) photon-gluon fusion.

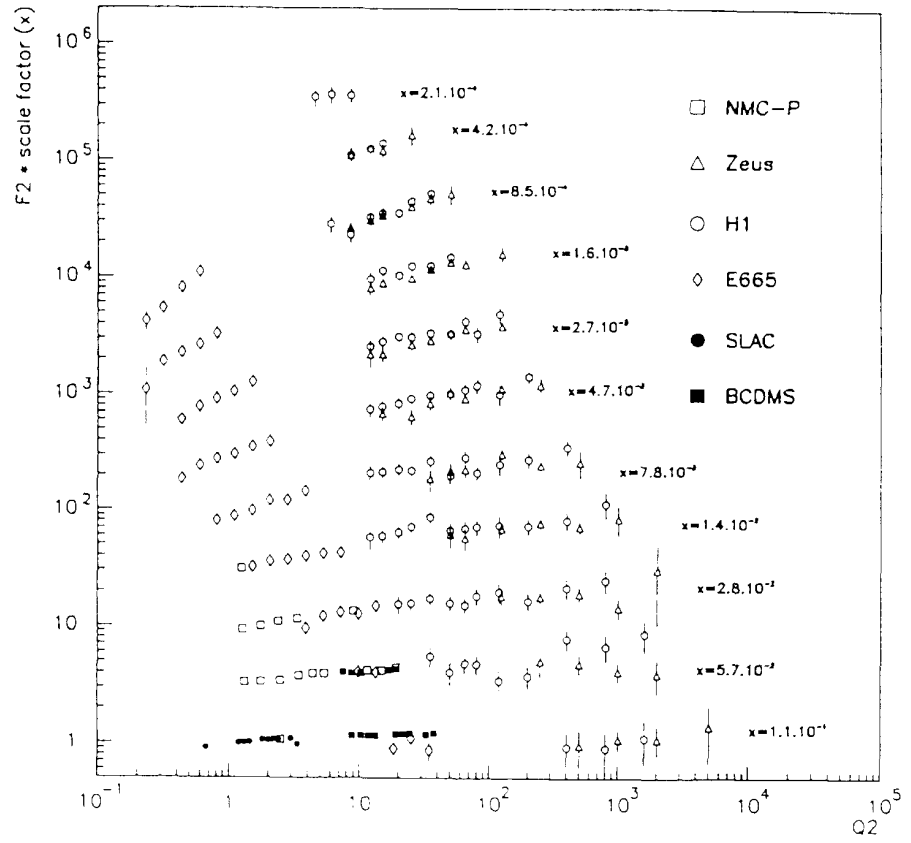

Fig. 17. $F_2(x, Q^2)$ at fixed x values as a function of Q^2 from different experiments. The data points of fixed target experiments have been slightly rebinned in x to match the HERA values.

$E_e = 26.7$ GeV, $E_p = 820$ GeV. Two general purpose detectors, H_1 and ZEUS, are taking data at luminosities $\mathcal{L} \sim 4 \times 10^{30}$ cm^{-2} s^{-1}. One of the main physics purpose of the experiments at HERA is the study of deep inelastic processes (DIS) [12]:

$$\text{Neutral current processes via } \gamma, Z^0 \text{ exchange:} \qquad \text{ep} \rightarrow \text{e}X \tag{20}$$

$$\text{Charged current processes via } W^{\pm} \text{ exchange:} \qquad \text{ep} \rightarrow \nu X \tag{21}$$

The processes and the kinematic variables are illustrated in Fig. 16. In the simple quark–parton model the current particle (γ, Z^0, $W^{\pm}$) emitted by the incoming electron interacts with one of the quarks of the proton. The scattered quark gives rise to a jet of hadrons (current jet). The proton remnants give rise to a second jet of hadrons (the target jet). The process may be described by the four momentum transfer squared Q^2 and by the energy transferred $\nu = E_e - E_{e'}$, or by a Bjorken scaling variable $x = x_B = Q^2/2m_p\nu =$ fraction of the proton momentum carried by the struck quark, and $y = Q^2/xs$.

The cross–section for deep inelastic ep scattering may be computed from the elastic electron–quark cross–section. In the quark–parton model the only unknown is the probability $q(x)$ for finding a quark q in the proton carrying a fraction x_B of

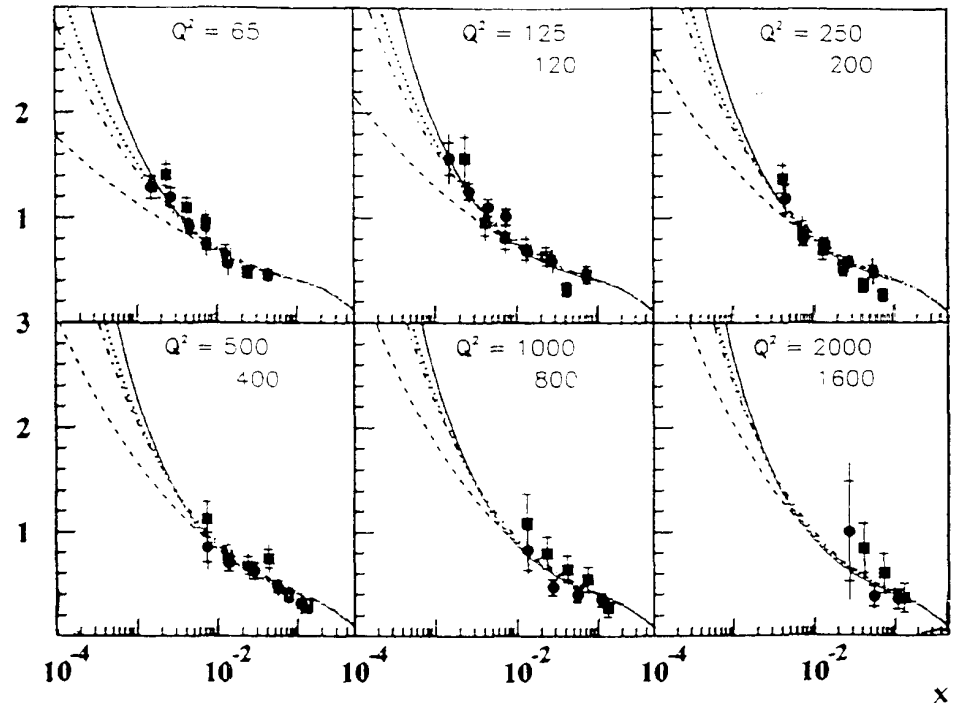

Fig. 18. The proton structure function F_2 from H1 and ZEUS versus x_B for various values of Q^2.

the proton momentum. The structure function F_2^p is given by $F_2^p = \sum e_q^2\, q(x)$. In this approximation F_2 is independent of Q^2 (Bjorken scaling). For NC deep inelastic scattering one has

$$\frac{d\sigma(\mathrm{ep} \to \mathrm{eX})}{dx\; dQ^2} \simeq \frac{4\pi\alpha^2}{Q^4}\frac{1}{x}\left(1 - y + \frac{y^2}{2}\right) F_2(x, Q^2) \tag{22}$$

Because of the new large c.m. energy, HERA allows to study the structure function F_2 at very small values of x and at very large Q^2 (provided enough luminosity is avaible). Fig. 17 shows a recent compilation of values of F_2 plotted versus Q^2 for different values of x. While the variation of F_2 with Q^2 (scale breaking) is not expected in the simple quark–parton model, it is predicted in QCD from gluon bremstrahlung and quark pair creation by gluons. The data are in agreement with this picture.

Fig. 18 shows that F_2 increases considerably at small values of x ($x < 0.01$) for any value of Q^2. This increase is predicted by perturbative QCD. According to Lipatov the gluon density in the proton at small x rises as $g(x) \sim x^{-(1+\lambda)}$, with $\lambda = \alpha_s(12 \ln 2)/\pi \simeq 0.5$.

It is worth recalling that deep inelastic data at lower energies have shown that for $x > 0.1$ one has dominance of u and d–quarks, with d quarks contributing about one half of u quarks. The data indicate that one half of the proton momentum is carried by gluons, which dominate for $x < 0.2$. The contributions from $\overline{q}$, resulting from $q\overline{q}$ pair creation by gluons is small and is concentrated at $x < 0.1$.

Even if gluons contribute 50% of the proton momentum, it is difficult to extract

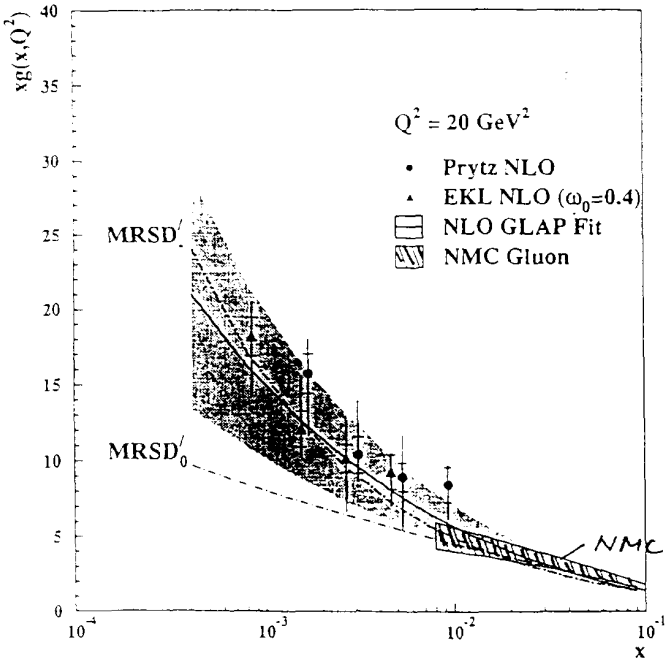

Fig. 19. The gluon structure function from the ZEUS and the NMC experiments for $x < 0.1$.

the gluon density function $g(x, Q^2)$ because gluons do not contribute directly to DIS in the quark–parton model, which corresponds to zeroth order QCD. At the next leading order one has scaling violations, which dominate at low x–values. One can extract the gluon structure function from the slope of $dF_2/d\ln Q^2$, obtaining the $g(x)$ plotted in Fig. 19. Thus the number of partons in the proton increases both at low values of x and at high values of Q^2, as sketched in Fig. 20. This means that when we are looking inside the proton with a better resolution (a "large magnifying glass") we see more partons and the number of gluons tends towards a large value.

7.2. Photoproduction. Diffractive processes

The process studied is $e+p \rightarrow e_{tag} + X$, where e_{tag} is measured in a calorimeter at small angles. The c.m. energy of γp collisions is $W^2_{\gamma p} = (E_e - E_{e'})s/E_e$. From the diagram of Fig. 16a, neglecting Z^0 exchange, one may say that the DIS cross–section may be expressed in terms of the flux of virtual photons times the cross–section $\sigma_{tot}(\gamma^* p)$ for scattering a virtual photon γ^* on protons

$$F_2(x, Q^2) \simeq \frac{Q^2(1-x)}{4\pi^2\alpha}\sigma^{\gamma^* p}_{tot}(x, Q^2). \tag{23}$$

A compilation of photoproduction data, including real photons at low energies and virtual photons at high energies, is shown in Fig. 21. It indicates that the high–energy total γp cross–section rises with c.m. energy, like the hadron–hadron cross–sections. The optical theorem allows to compute from σ_{tot} the elastic scattering cross–section σ_{el}, which rises even faster with energy.

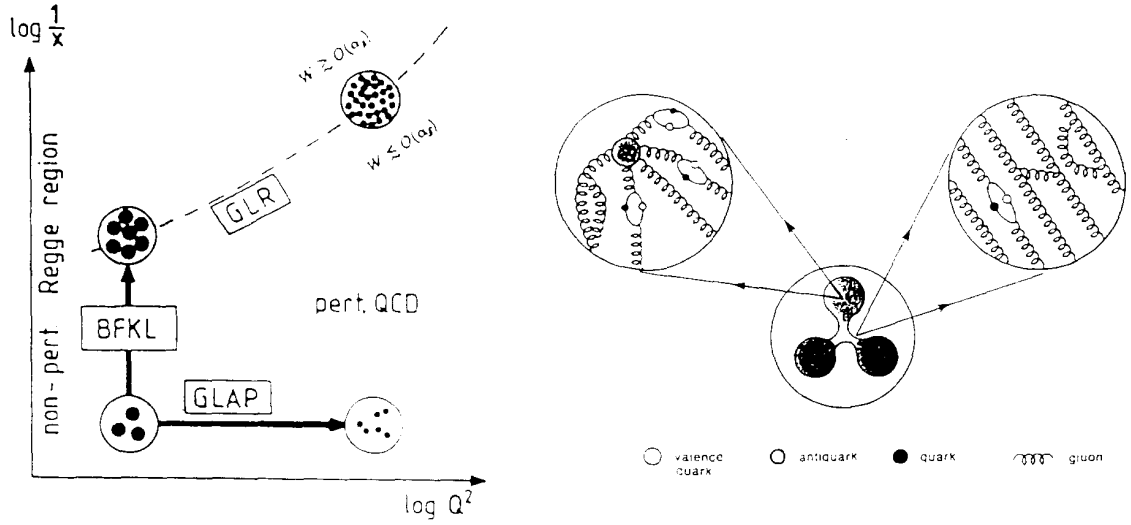

(a) (b)

Fig. 20. (a) Schematic evolution of the quark densities in various (x, Q^2) regions according to the main dynamical effects. (b) Schematic nucleon structure. Center: the nucleon made of three constituent quarks interacting via colour force tubes. Left: a close up reveals the sea of virtual particles around the valence quarks. Right: a close up of a colour tube reveals the gluons that carry the colour force, and which can fluctuate into $q\bar{q}$ pairs.

The elastic virtual γp scattering is difficult to detect experimentally. One can instead detect a class of DIS events which shows diffractive behaviour. These events are characterized by a large rapidity gap; they contribute a few % to F_2.

8. Others

Among the very many results obtained in fixed target experiments at accelerators, we shall single out and mention very briefly only the study of DIS with longitudinally polarized μ^- and e^- on protons in sophisticated experiments at CERN (SMC with muons) and at SLAC (E142, E143 with electrons). After precision checks on the Bjorken sum rule for $\vec{\sigma_p} - \vec{\sigma_n}$, the experiments measured the spin dependent function $g_1(x)$ which depends on experimentally measured asymmetries. All experiments found, in the absence of effects from the axial anomaly, that only 30 % of the proton spin is carried by the valence quarks. It is not yet clear where does the main part of the proton spin come from. A fraction seems to be carried by the strange sea quarks.

9. Conclusions

A wealth of information has been obtained by high-energy colliders and lower energy fixed target accelerators. e^+e^-, $\bar{p}p$ and ep colliders provide several complementary information on parton-parton interactions. e^+e^- interactions produce well defined parton final states and seem to be the best suited to perform precision measurements of the electroweak and strong parameters. Deep inelastic scattering in ep collider seems to be the best way to study the partonic structure of nucleons. The $\bar{p}p$ collider offers the means to reach the highest parton-parton energies and to search

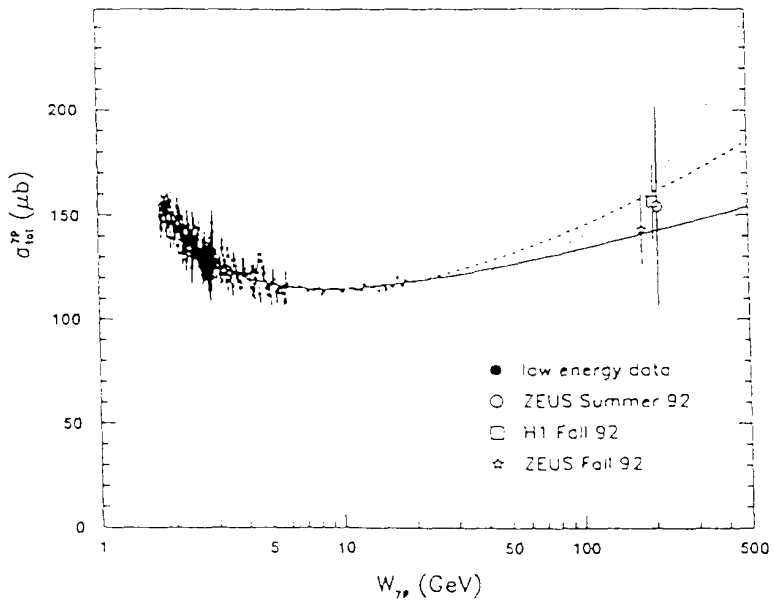

Fig. 21. Total γp cross-section versus c.m. energy, including the "indirect measurements" at HERA.

for the most massive particles. Fixed target experiments have provided many new results as exemplified by the study of the spin structure of the proton, of possible neutrino oscillations, of CP violation studies, etc. Many of the collider results are of interest in the field of high-energy particle astrophysics.

As for the future: the LEP c.m. energy is being raised to 140 GeV, and should reach 190 GeV in 1996. This will open the possibility of studying processeses of the type $e^+e^- \to W^+W^-$. HERA is expected to increase its luminosity by two orders of magnitude, thus really opening up the field of large Q^2. They also plan to operate with polarized electrons. FNAL is planning to increase the luminosity by at least an order of magnitude. In the far future LHC will provide $\sqrt{s}$=14 TeV and high luminosities.

It may be worth pointing out that high-energy physics experiments have changed significantly in the last 20 years: moving away from small single-purpose detectors, to large highly-complex multipurpose detectors. This trend has also changed the sociology of this field of research, with many collaborating groups from different institutions, each group comprising many physicists, students, engineers and technicians.

It is interesting to comment on the relation between high-energy physics and the early Universe. The energies achieved in the e^+e^- collisions at LEP correspond to those prevailing 10^{-10} s after the Big Bang. The establishment of the existence of only three quark-lepton families has profound implications for the nucleosynthesis of light elements, which took place 200 s after the Big Bang.

We would like to thank the members of the OPAL Collaboration for their co-operation. We thank the staff of the CERN Scientific Editing Services for their

highly-professional work.

10. References

1. LEP Electroweak working group, *A combination of preliminary LEP electroweak results for the 1995 summer conferences*, LEPEWWG/95-02 (1995).
2. M. Schnelling, *QCD results from the study of hadronic Z-decays*, CERN/PPE 94-184 (1994).
3. M.F. Watson, *Quark and gluon jet differences at LEP*, OPAL-CR202 (1995).
4. SLD Coll., K. Abe et al., Phys. Rev. Lett. **73** (1995) 25.
5. G. Giacomelli, *Hadron-hadron elastic scattering and total cross section at high energies*, DFUB 9/94 (1994).
6. UA4/2 Coll., C. Augier et al., Phys. Lett. **B316** (1993) 448; **B344** (1995) 451.
7. E710 Coll., N. Amos et al., Phys. Lett. **B243** (1990) 158; **B301** (1993) 313.
   CDF Coll., F. Abe et al., Phys. Rev. **D50** (1994) 5550; **D50** (1994) 5518.
8. M.M. Block et al., Phys. Rev. **D47** (1993) 101; NUHEP-490 (1995).
   A. Donnachie and P.V. Landshoff, Phys. Lett. **B296** (1992) 227.
9. A.D. Krisch, Nucl. Phys. Suppl. **25B** (1992) 285.
   D.G. Crabb et al., Phys. Rev. Lett. **65** (1990) 3241.
10. CDF Coll., F. Abe et al., Phys. Rev. Lett. **68** (1992) 1104.
    D0 Coll., S. Abachi et al., Preliminary (1994).
11. CDF Coll., F. Abe et al., Phys. Rev. Lett. **73** (1994) 225; **74** (1995) 2626.
    D0 Coll., S. Abachi et al., Phys. Rev. Lett. **74** (1995) 2632.
12. G. Wolf, *HERA Physics*, DESY 94-022 (1994).
    G. Wolf, *Physics with colliders*, CERN 95-04 (1995).